Development of Whispering Gallery Mode Resonators in Lithium Niobate

A thesis submitted in partial fulfillment of the requirement
for the degree of Bachelor of Science
Physics from the College of William and Mary in Virginia

by

David J. Gribbin V

Accepted for: BS in Physics

_____

I. Novikova

_____

W. J. Kossler

Williamsburg, Virginia
May 2011

Abstract

The goal of this project is to determine the best fabrication and coupling techniques for the production of lithium niobate Whispering Gallery Mode Resonators (WGMRs) to be used in the generation of the second harmonic. I used a lathe, diamond sandpaper, and simple polishing techniques to fabricate WGMRs in the form of a disk with a rounded edge. I have fabricated a lithium niobate WGMR with surface imperfections no greater than $.5\mu$m that has a Q Factor of $2.2 * 10^7$. Using prism-to-disk coupling, I have coupled a 795nm laser to the WGMRs. We have also observed the second harmonic. In the future we hope to use these WGMRs to produce squeezed light and heralded single photons.

1 Introduction

A whispering gallery is a gallery beneath a dome, vault, or enclosed in a circular or elliptical area in which whispers can be heard clearly in other parts of the building [4]. The whispers reflect along the curved walls of the structure, reaching the listener with little reduction or distortion. In the same way sound reflects along the wall of a dome or vault, whispering gallery mode resonators (WGMRs) reflect light along their outer surface.

Using total internal reflection, circular WGMRs propogate light along its curved surface allowing the light to interfere with itself and create an optical cavity. In a traditional Fabry-Perot cavity, the intensity inside the cavity relative to the input laser increases with the quality factor, or Q factor. However, reflecting mirrors of the Fabry-Perot cavity limit the amount of light captured inside the cavity; most of the light reflects off the first reflecting mirror. The WGMR captures light into the cavity through evanescent wave coupling, an advantage over the Fabry-Perot cavity, allowing for a much greater percentage of the initial light to be captured into the cavity while maintaining a large Q factor. This results in a higher light intensity inside the WGMR than the Fabry-Perot.

This project requires coupling horinzontally polarizared single mode 795 nm laser light into a lithium niobate WGMR. Lithium niobate is used because it is birefringent and will thereby allow for second harmonic generation. The better the Q factor, and accordingly the more intense the field inside the WGMR, the more second harmonic is generated.

The overall goal of this project is to determine the most effective way to manufacture and couple high Q factor WGMRs in lithium niobate for the future purpose of second harmonic generation. This paper describes the following: theories underlying the WGMR fabrication and coupling in section 2, WGMR fabrication in section 3, results of WGMR fabrication in section 4, WGMR coupling in section 5, and the results of WGMR coupling in section 6.

2 Theory

2.1 Cavity Properties

An optical cavity or optical resonator is any structure that light can travel inside of and interfere with itself. The Fabry-Perot cavity is commonly described as two mirrors set parallel to each other with specific transmission and reflection coefficients. A laser shone perpendicular to the face of the first mirror will transmit a portion of the laser's intensity into the region between the two mirrors. The remnant laser intensity then strikes the second mirror with most of it reflecting back towards the first mirror where it interferes with itself. In especially high finesse cavities, both mirrors have very high reflection coefficients and very low transmission coefficients. In such cavities it becomes difficult to generate a high intensity field inside the Fabry-Perot cavity because most of the incident light reflects off the first mirror.

WGMRs take advantage of evanescant wave coupling and have significantly higher interior field intensity. The intensity inside the cavity vs the incident intensity is calculated using the equation below [1]:

$$\frac{P_{cav}}{P_{in}} = \frac{T_1}{|1 - \sqrt{R_1 R_2 e^{-\alpha p}}|^2} \tag{1}$$

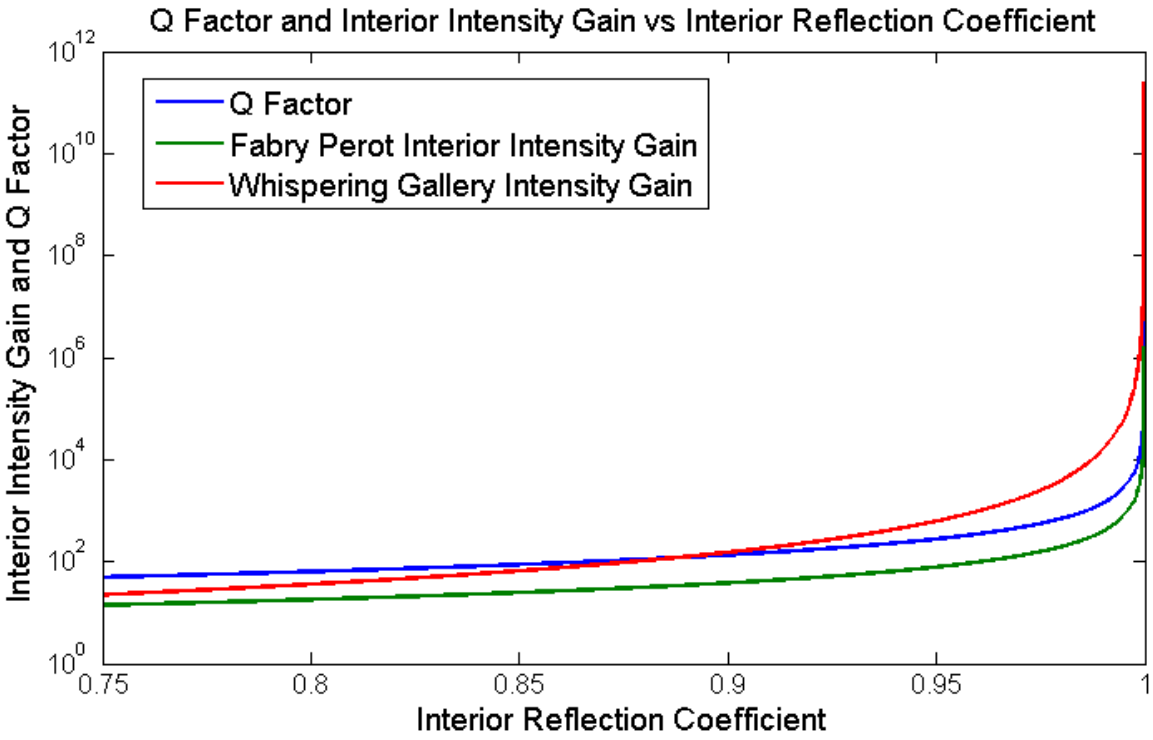

Figure 1: Intensity Inside WGMR, Intensity Inside Fabry-Perot, and Q Factor of both Cavities vs Interior Reflection Coefficient (R1)

In modeling the Fabry-Perot cavity vs the WGMR, I assumed that both cavities were lossless and set α=0. I also set R_2 to 1, assuming a perfectly reflecting second mirror in the Fabry-Perot cavity and total internal reflection in the WGMR. The Fabry-Perot cavity's transmission coefficient T_1 decreases as R_1 because in a Fabry-Perot cavity $T_1 + R_1 = 1$. In a WGMR T_1 is constant at .4, the highest coupling percentage I achieved. Figure 1 shows how the constant transmission coefficient in the WGMR has a clear advantage over the variable transmission coefficient in the Fabry-Perot cavity.

Evanescent wave coupling allows WGMRs to couple light into a cavity with a very high reflection coefficient and retain a high transmission coefficient, resulting in a higher interior intensity. The higher intensity allows for greater second harmonic generation.

2.2 Evanescent Wave Coupling

The equation for an evanescent wave is determined by assuming a transmitted wave at a boundary condition and solving Maxwell's equations. In a two dimensional space, x and z, the assumed transmitted wave is described as:

$$\vec{k}_T = k_T(\sin\theta_T x + \cos\theta_T z) \tag{2}$$

$$k_T = \omega n_2 / c \tag{3}$$

Using the common approximation and represent the assumed transmitted wave at the boundary as a plane wave:

$$\tilde{\mathbf{E}}_T(\vec{r}, t) = \tilde{\mathbf{E}}_{0_T} e^{i(\vec{k_T} - \omega t)} \tag{4}$$

Fully expand transmitted wave:

$$\tilde{\mathbf{E}}_T(\vec{r}, t) = \tilde{\mathbf{E}}_{0_T} e^{i(k_T(\sin\theta_T x + \cos\theta_T z) - \omega t)} \tag{5}$$

Account for the imaginary wave with trigonometric identity:

$$\tilde{\mathbf{E}}_T(\vec{r}, t) = \tilde{\mathbf{E}}_{0_T} e^{i(k_T(\sin\theta_T x + i\sqrt{\sin^2\theta_T - 1} z)\cdot\vec{r} - \omega t)} \tag{6}$$

$$\tilde{\mathbf{E}}_T(\vec{r}, t) = \tilde{\mathbf{E}}_{0_T} e^{-k_T\sqrt{\sin^2\theta_T - 1}\ z}\ e^{i(k_T \sin\theta_T\ x - \omega t)} \tag{7}$$

Resulting evanescent wave:

$$\tilde{\mathbf{E}}_T(\vec{r}, t) = \tilde{\mathbf{E}}_{0_T} e^{-\frac{\omega}{c}\sqrt{n_1^2 \sin^2\theta_I - n_2^2}\ z}\ e^{i(\frac{\omega n_1}{c}\sin\theta_I\ x - \omega t)} \tag{8}$$

This evanescent wave is also found experimentally. Note that the resulting evanescent wave exponentially decreases in the z direction while propagating in the +x direction. Also note that the angle of incidence, θ_I, is important in determining the intensity of the evanescent wave. In the final evanescent wave soluiton the θ_I is 90-θ described in Figure 2.

In this experiment I couple 795nm laser light into the WGMR using a rutile (TiO_2) prism. The prism is necessary because it has a higher index of refraction than lithium niobate ($LNbO$). The index of refection for TiO_2 and $LNbO$ is 2.52 and 2.257. The coupling prism allows the laser to propagate along the rim of the WGMR. Without the coupling prism the laser would enter the WGMR at an angle. Snells Law

$$\sin\theta_T = \frac{n_1}{n_2}\sin\theta_I \tag{9}$$

allows us to find the correct angle for the most intense evanescent wave. With the laser inside the prism at the point of total internal reflection, the angle of the laser reflected off the face of the prism relative to the initial laser path, ϕ, is given by:

$$\phi = \arcsin(\frac{n_{prism}}{n_{air}}\sin((\arcsin(n_{disk}/n_{prism}) - 45°)))/2 \tag{10}$$

The evanescent wave is generated from the surface of the coupling prism and interacts with the WGMR. A graphical depiction of the evanescent wave and its coupling into a WGMR is shown below in Figure 2.

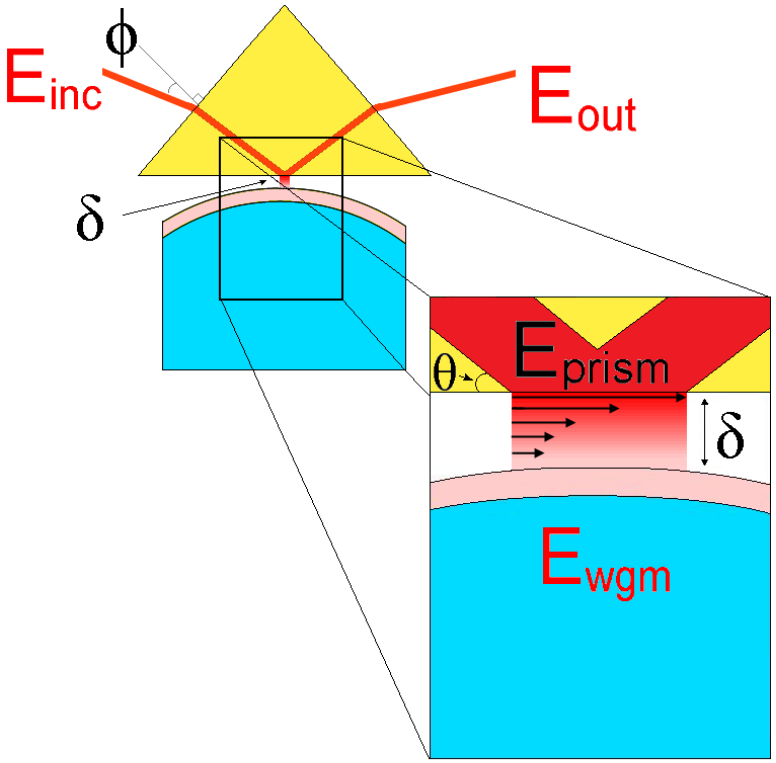

Figure 2: Evanescent Wave Coupling

After entering the coupling prism, the incident wave (in red) totally internally reflects off the hypotenuse of the prism (in yellow). The englarged section shows how

the evanescent wave, emitted from the coupling prism, propagates in the +x direction while decreasing in the -z direction. The evanescent wave loses intensity, turning from red to pink, and at a certain distance the evanescent wave couples with the WGMR (in blue). The distance from the coupled WGMR to the prism, the skin depth, is indicated by δ.

The evanescent wave does not reflect off the surface of the WGMR because each wave moving in the +x direction is generated along the -z axis. The light coupled to the WGMR has been generated inside of the WGMR by the evanescent wave, bypassing any reflection off the surface. That is why it is possible to model the WGMR as having a constant transmission coefficient. Now matter how well polished the disk is, and alternatively how high the R_1 value is, the WGMR can evanescently couple with the same transmission coefficient.

2.3 Quality Factor

The level of intensity gain inside the WGMR is determined by the Q factor of the WGMR. The Q factor is described as:

$$Q = \frac{\nu_0}{\Delta\nu} \tag{11}$$

ν is the frequency of the incident wave and $\Delta\nu$ the full width at half-max. The full width at half-maximum is the width of the inverted power spike in frequency space at half its maximum. A measurement of the Q factor is shown below (Note: the x axis, time, can also be considered frequency because the laser is scanning over frequency at a set rate):

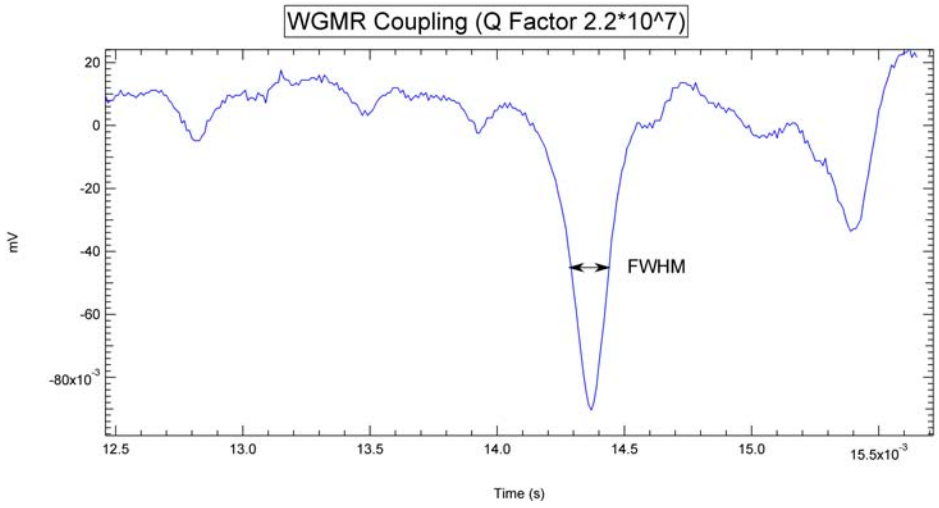

Figure 3: A Measurement of the Q factor. (X-axis-laser frequency is scanned at the rate of 5.94 GHz/s)

The Q factor is also defined as:

$$Q = \frac{F \cdot \lambda \cdot 2 \cdot n \cdot L}{c} \tag{12}$$

Where F is the Finesse shown below [3]:

$$F = \frac{FSR}{\Delta\nu} = \approx \frac{\pi}{2\arcsin(\frac{1-\sqrt{L}}{2\sqrt[4]{L}})} \tag{13}$$

These expressions predict the Q factor for a cavity of a certain index of refraction, n, and path length, L, for a particular frequency λ. These Q factor predictions do not take into account losses due to surface imperfections or absorbtion and serve as an upper limit for what is an experimentally achievable Q factor.

3 Experiment

My experimental procedure is divided into WGMR fabrication and WGMR coupling. The fabrication section describes the methods used to fabricate high Q factor WGMRs in lithium niobate. These methods include basic procedure and surface damage troubleshooting. Coupling procedure includes laser lab setup and various coupling techniques.

3.1 WGMR Fabrication

The process of fabricating WGMRs begins with cutting a disk of lithium niobate from a solid sheet with a diamond bore out drill bit. The drilling process leaves the circumference of the lithium niobate disk very rough. The outer rim must be polished because any imperfections along the outer rim lowers the Q factor.

To begin polishing, the lithium niobate disk is mounted on a small lathe as shown in Figure 4.

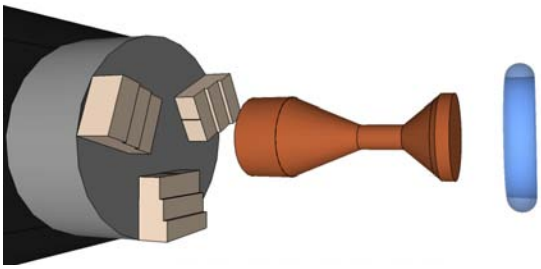

Figure 4: Chuck Jaws, Brass Mount, Lithium Niobate Disk

Figure 5: Polishing on Lathe by Hand

A hot mounting wax from Allied High Tech Products holds the disk to the surface of the brass mount. Different mounts are used for different sized disks and all the mounts milled by hand on the lathe. Larger mounts have more surface area and hold more mounting wax, thereby preventing the disk from flying off during polishing. To attach the disk on the mount, I heat the brass mount with a heat gun, apply a small amount of mounting wax, and place the disk on the mount. The residual heat from the brass mount will heat the disk and allow the mounting wax to bond to both the mount and the disk. While the wax is still warm, I attempt to center the disk.

Centering the disk is done by hand. It is not necessary that the disk be perfectly centered because elliptical disks behave similarly to perfectly circular disks [2]. Polishing on the lathe will remove some ellipticity.

Different stages of sandpaper are used to generate a fine polish. Polishing with 600, 1000, and 1200 grit aluminum oxide sandpaper (the type sold at hardware stores) shape the disk to either a peaked or broad edge profile. Strips of aluminum oxide sandpaper are cut and pressed at parts of the disk to shape the edge profile. Small amounts of water must be added to help carry away the lithium niobate dust. Currently the brass post constricts the sharpness of the edge profile because the post interferes with the sandpaper while polishing.

After achieving the desired profile with the aluminum oxide sandpaper, diamond sandpaper is used. The s of the diamond sandpaper are 9μm, 3μm, 1μm, $.5\mu$ m, and $.1\mu$ m. The diamond sandpaper is used because the granule size is much more consistent than aluminum oxide alternatives. A polishing solvent is used while sanding with diamond sandpaper to prevent diamond sandpaper from accumulating lithium niobate dust and ceasing to polish the WGMR. While polishing times are not exact, polishing two minutes at each of these stages will provide a surface with imperfections no greater than 1μm in the critical area.

Surface damage can occur while polishing. To avoid this, it is important to clean the disk after every sanding stage, especially after using the aluminum oxide sandpaper. The alumimum oxide particles have a tendency to flake off and gather along the disk and the mount. At finer sanding stages the oil will carry these particles into the area where the sandpaper is contacting the disk, generating long gouges in the surface of the disk. Damage due to contact while moving the disk may also occur. Note: often the oil will bead in small divots at the surface of the disk making surface imperfections appear $\approx 3 - 30$ times larger than they are when when dry. Blowing air on the disk or rotating it at high speeds with the lathe will remove the excess polishing solvent.

Viewing the disk between polishing stages prevents significant surface damange from going unnoticed until the finer stages, where the fine diamond sand paper cannot remove the large imperfections. My setup for viewing with the HIROX KH-3000VD High Resolution Digital-Video Microscopy System is shown below. The setup allows for rotation of the disk to search the entire circumference of the disk for imperfections.

The high quality polish combined with optimal coupling creates an ultra-high Q factor cavity. The finished disks are 3-5mm in diameter and $\approx$ 1mm wide.

Figure 6: Gouges Due to Aluminum Oxide Residue

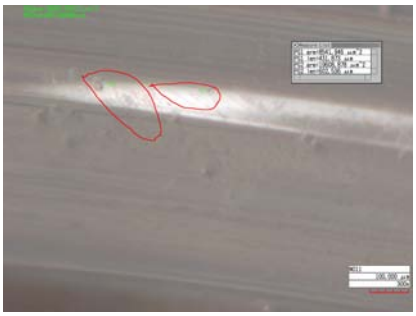

Figure 7: Surface Imperfections Due to a Fingerpad

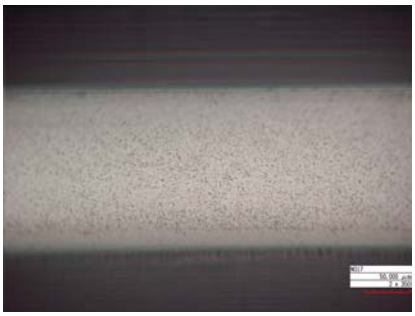

Figure 8: Polishing Oil Collecting in Small Divots

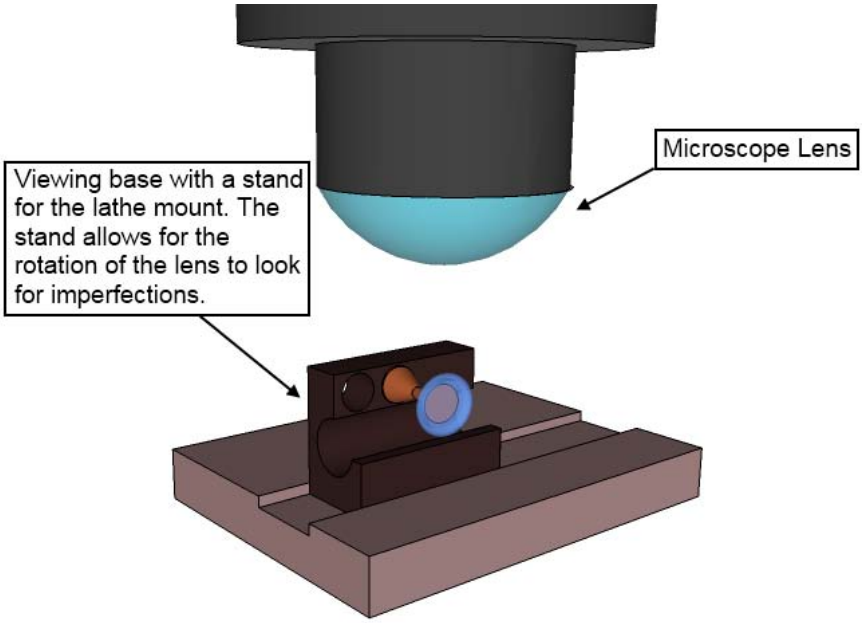

Figure 9: Hirox Viewing Mount

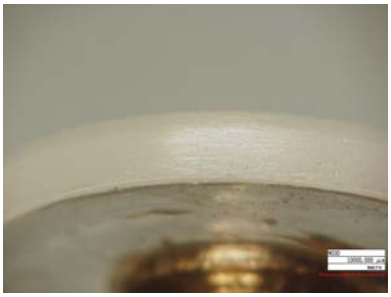

Figure 10: Broad Edge Profile after 600 grit Aluminum Oxide Sandpaper

4 WGMR Fabrication Results

4.1 Polishing setup

Developing the most efficient polishing setup was one part of my research. Operating a mini-lathe at one third total power, shown on the proceeding page in Figure 11, produced highly polished WGMRs. While polishing times are not exact, polishing two minutes at each of the sanding stages will provide a surface with imperfections no greater than 1μm in the critical area. An image of the diamond sandpaper used is shown on the next page in Figure 12. Wrapping the sandpaper around the disk

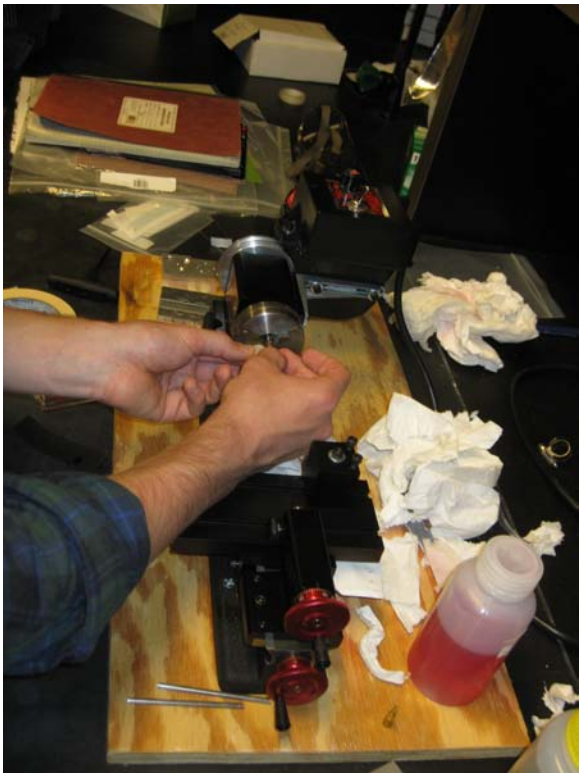

Figure 11: Polishing on the Mini-Lathe

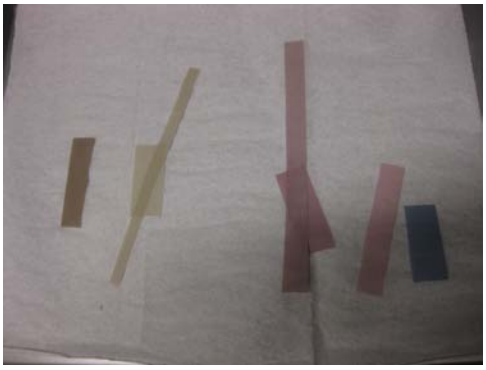

Figure 12: Strips of Diamond Sandpaper

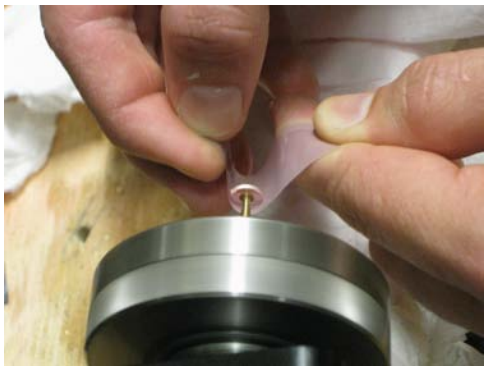

Figure 13: Wrapping Diamond Sandpaper

while polishing, shown on the proceeding page in Figure 13, instead of polishing with the diamond sandpaper taut, polishes the disk faster and more evenly. Currently, the mounting setup works well; however, the post may cause the experimenter to grind an edge profile that is not totally in the center of the disk. No ill effects have been observed from having an off center edge profile.

4.2 Polished disks

I fabricated five WGMRs, three out of stoichoimetric lithium niobate and two out of magnesium doped lithium niobate. The first stoichoimetric lithium niobate disk has a very sharp edge profile with a critical coupling area on the order of 157μm, shown in Figure 14. The other disks had much greater critical coupling areas due to a broader edge profile, an example shown in Figure 15. I found that the stoichiometric lithium niobate was less brittle than the magnesium doped lithium niobate because the critical area in magnesium doped lithium niobate would flake off when sharp edge profiles were attempted. The advantages and disadvantages of different edge profiles are not clearly understood at this time.

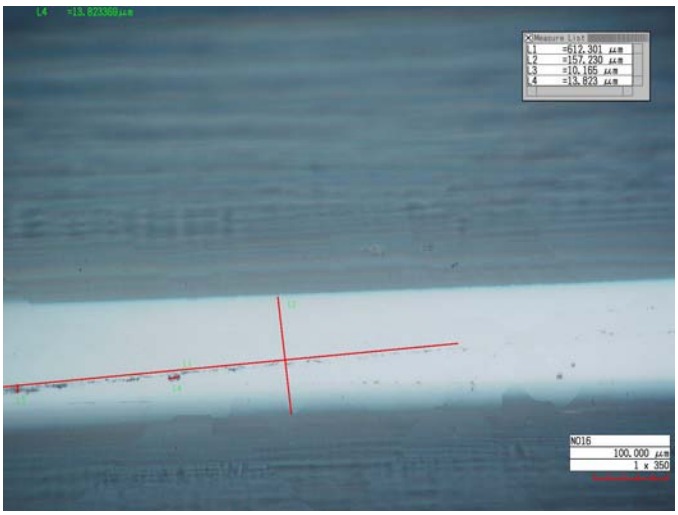

Figure 14: Sharp Stoichoimetric Lithium Niobate (Critical area=157μm)

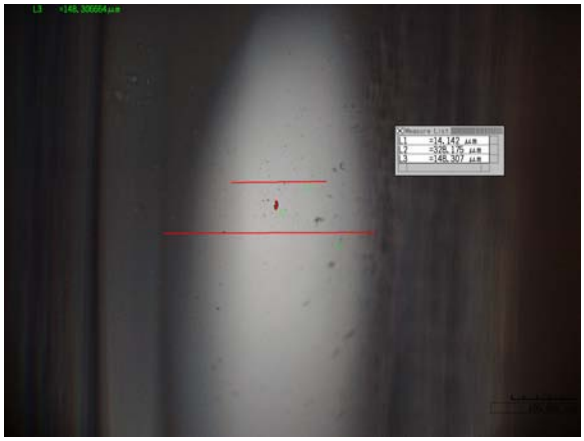

Figure 15: Broad Magnesium Doped Lithium Niobate (Critical area=328μ)

The scratch or dig number is 1,000 times the width of the largest scratch or 100 times the diameter of the largest dig. The best scratch dig number I achieved was 48μ, a dig with a diameter of .48μm. An image at the surface of the best polished disk is shown below at 2,800X. The objects out of focus in the image is polishing liquid residue and lithium niobate dust.

5 WGMR Coupling

5.1 Coupling setup

As shown in the figure above, the coupling setup has three main sections. The first section, enclosed in blue, includes the laser emitter, polarizing beam cube, alignment mirrors, and single mode fiber optic cable. This part of the setup horizontally polarizes the light and passes it into the single mode fiber optic cable.

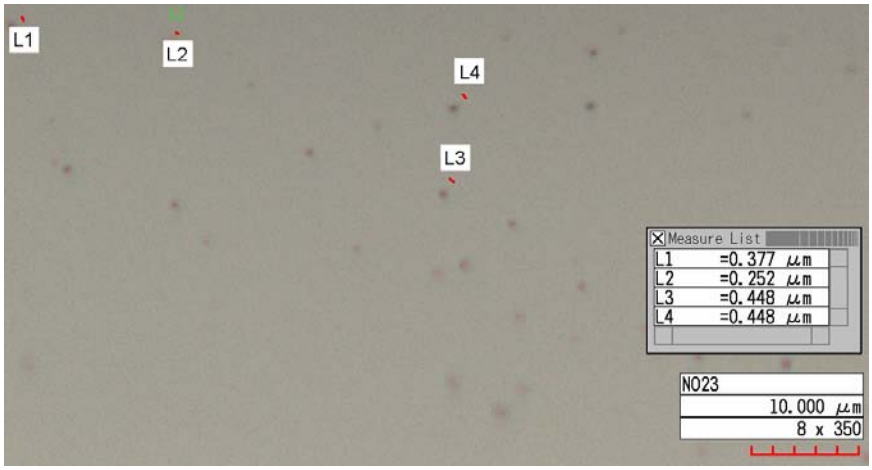

Figure 16: Best Polished Disk

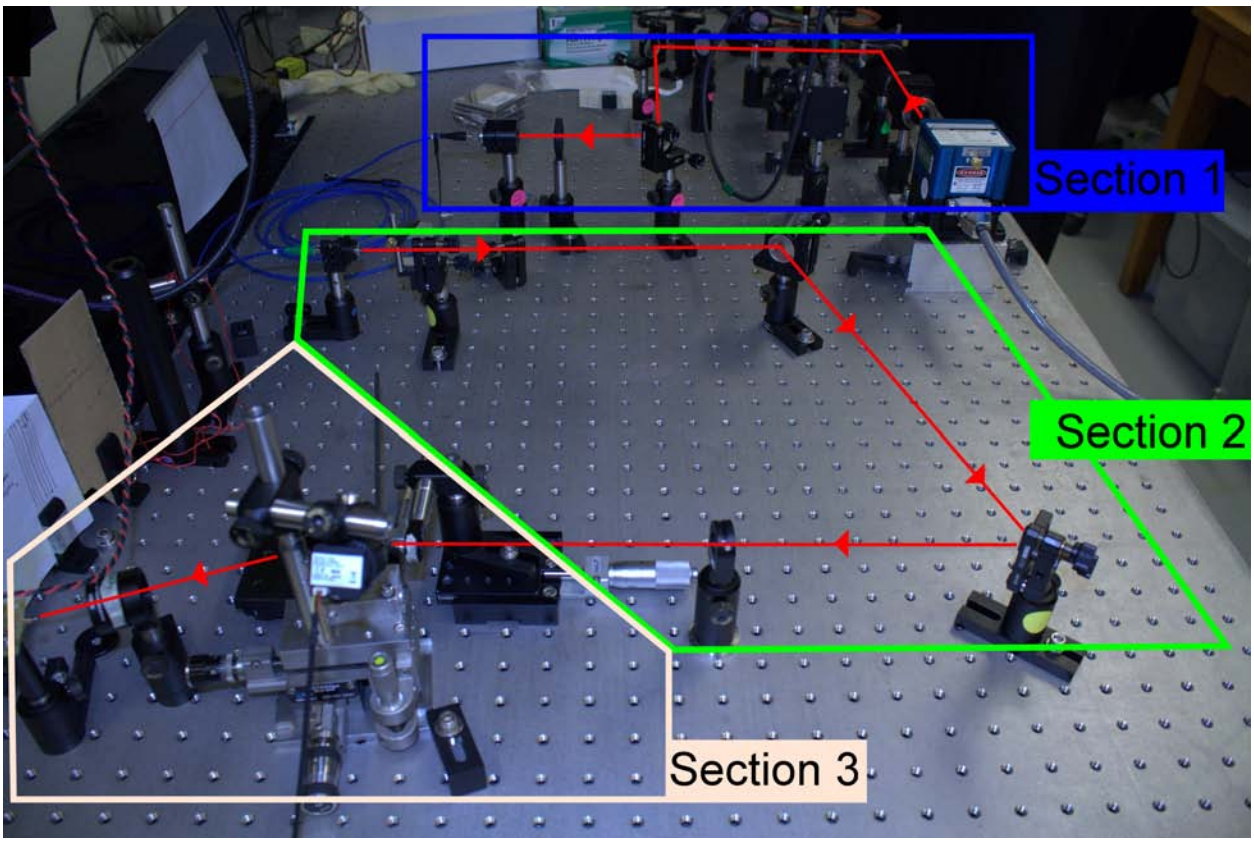

Figure 17: Coupling Lab Setup

The second section of the setup, enclosed in chartreuse, prepares the laser beam for prism-to-disk coupling. The laser passes through another polarizing beam cube, is

reflected by the alignment mirrors, and is modulated by an iris.

The third section of the setup, enclosed in white, includes the focusing lens, focusing lens modulation platform, WGMR modulation stage, coupling prism, coupling prism modulator, WGMR, infrared coupling camera, exit beam collimator, exit beam focusing lens, and photodiode. The spot size of the laser and the evanescent wave characteristics are changed by different focusing lenses. The coupling prism is made of rutile and has an index of refraction of 2.52. The WGMR is made of stoichiometric lithium niobate and has an index of refraction of 2.257. The infrared coupling camera is mounted to a CRT television and focuses on the hypotenuse of the rutile prism. The infrared camera lets the experimenter improve the early stages of coupling by optimizing the amount of laser light seen entering the WMGR.The exit beam collimator and the exit beam focusing lens allow for changes in the position of the pre-coupling laser without moving the post-coupling laser off the photodiode.

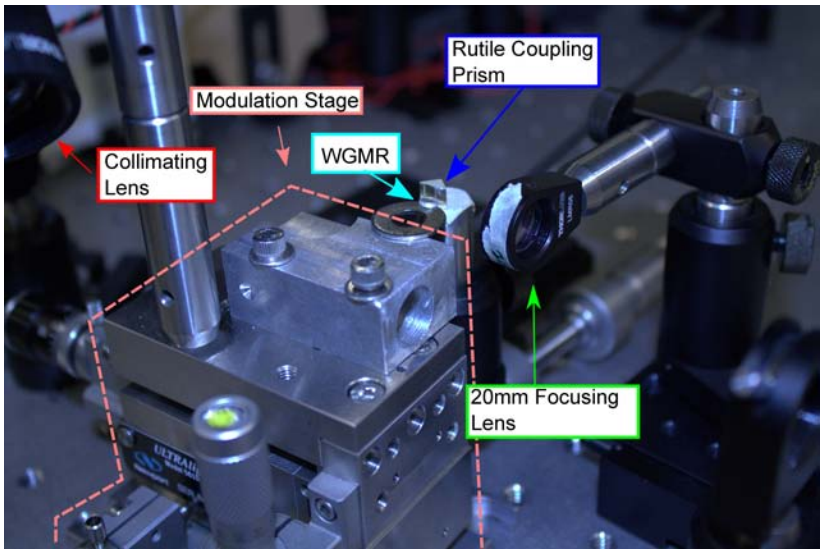

Figure 18: Coupling Setup: top view

Figures 17 and 18 show the setup of section 2 from different viewpoints. In Figure 17, the modulation stage used to move the WGMR is shown. The WGMR is mounted to a washer and is almost touching the rutile coupling prism. The rutile prism is mounted on a modulation stage that moves the prism towards and away from the beam path. The 20mm focusing lens is mounted on a modulation stage, also best seen in Figure 18, that moves the focusing lens along the beam path. The collimating lens is indicated in both figures. The infrared coupling camera is shown in Figure 18.

5.2 Prism-to-Disk Coupling

The WGMR is mounted to a modulator stage that brings the WGMR in contact with the rutile prism. There are four main parts to coupling: laser leveling, correct angle of incidence, WGMR resonator alignment, and laser position optimization. The laser

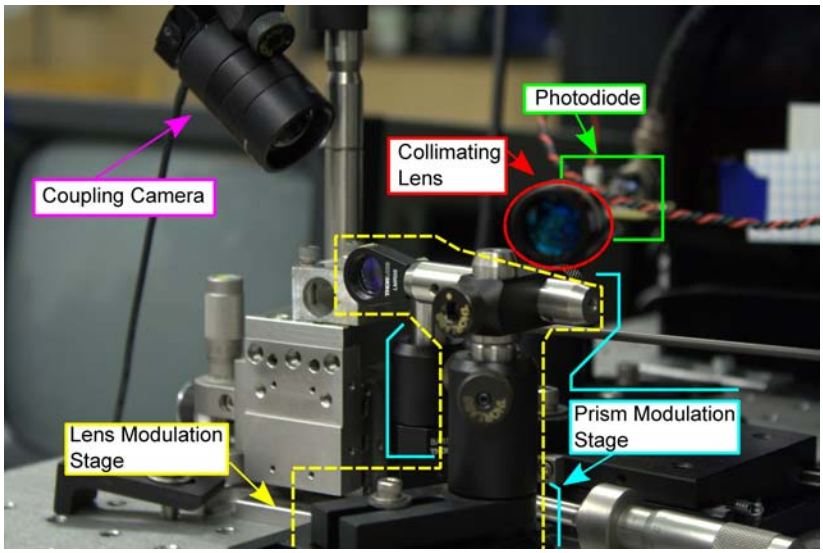

Figure 19: Coupling Setup: side view

is made level with the table and perpendicular to the plane of the focusing lens. After leveling the laser, the angle of incidence is measured by the angle the reflection off the surface of the prism makes with the incident laser beam. The WMGR couples with the evanescent wave emitted from the hypotenuse of the prism when the WGMR is 'correctly' placed on the first reflection point the laser makes in the prism.

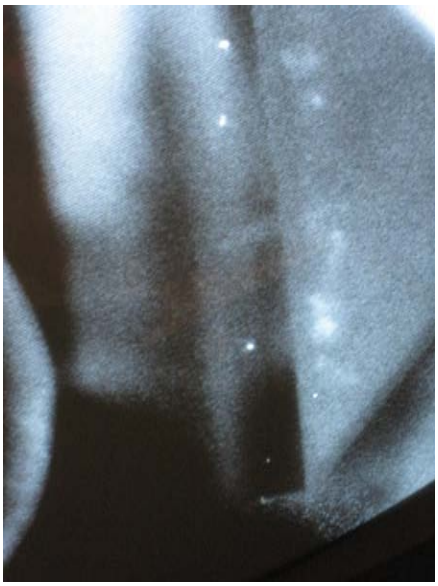

Figure 20: WGMR and Rutile Prism; No Coupling

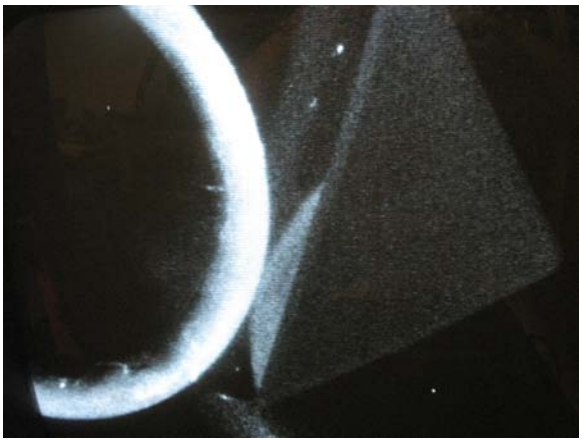

Figure 21: WGMR and Rutile Prism; Coupling

Correctly is defined by whether coupling occurs or not. (Figures 20 and 21 show lack of coupling and coupling) Many points in the general area of the first reflection point must be tested in a grid type fashion to find coupling, which is very time consuming. The initial coupling is optimized by adjusting the two reflecting mirrors. This changes the height, depth, and angle of the laser. The best laser position is the laser position that produces the best Q factor. When the optimal laser position is not in the exact center of the focusing lens, the position of the focusing lens is another factor that must be optimized for the best Q factor. The best coupling occurs when the laser position, angle of incidence, WGMR position, focusing lens position, and spot size are optimized.

6 WGMR Coupling Results

6.1 Coupling Percentage

After testing many different points of coupling with different angles of incidence, I determined that the best ϕ, indicated in Figure 2, the angle of incidence, is 53 degrees. The overall sample size of sharp disks and rounded disks is too small to make a definative statement about how the disk shape effected the coupling. A 20mm lens provided a minimum beam width of 5μm. The smaller beam widths provided better coupling, with 5μm providing the best. Modulations of the beam size with the iris had no effect on coupling percentage. The best coupling percentage achieved with this setup is 41 percent.

6.2 Q factor

The same setup used to obtain the highest coupling percentage was also used to find the best Q factor. Again, I cannot determine the effect of sharp or broad disks due to the small sample size. The iris had no effect on Q factor. Using the polishing and coupling setup outlined above, the best Q factor achieved is $2.2{*}10^7$. Figure 22 shows the data from the best Q factor observation.

All the data from the oscilloscope file are shown in box 1. The axes, mV and time, apply to the selected portion of box 1, box 2.

7 Conclusion

Using simple polishing techniques I was able to fabricate a WGMR in lithium niobate with a scratch dig number of 48μ. Using WGMRs fabricated in the method outlined in this paper, I was able to couple light into the WGMR and see a Q factor of $2.2 * 10^7$. Using these WGMRs we were able to see second harmonic generation. In the future, we hope to use the WGMRs to generate heralded single photons.

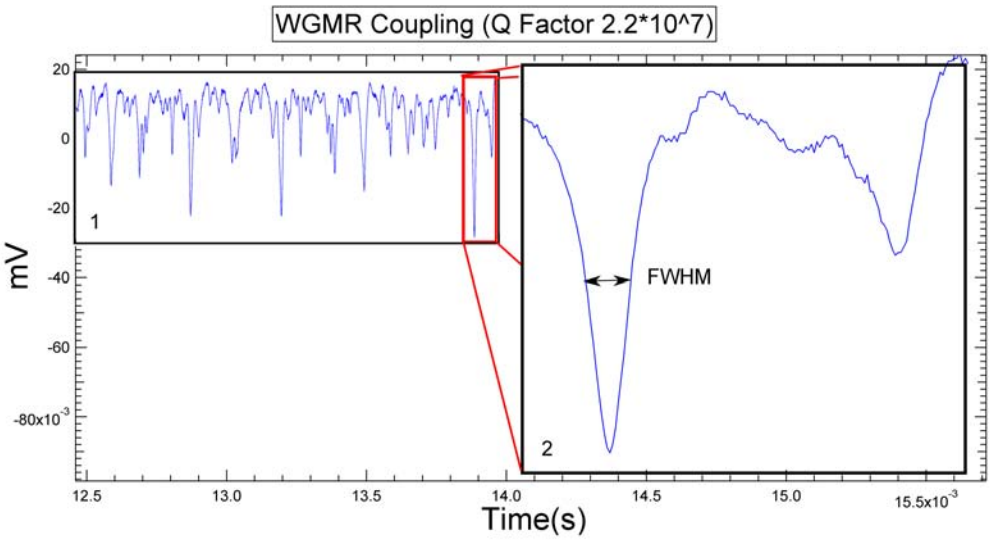

Figure 22: Q Factor Results. (X-axis-laser frequency is scanned at the rate of 5.94 GHz/s)

8 Acknowledgements

I would like to thank Irina Novikova for allowing me to work on this project and to thank Matt Simons for his continual assistance in all stages of the experiment. Also to Nate Phillips for questions concerning coupling theory and Gleb Romanov for his company.

References

[1] Hans-A. Bachor and Timothy C. Ralph. *A Guide to Experiments in Quantum Optics*. Wiley-VCH, 1998.

[2] Andrey B. Matsko. *Practical Applications of Microresonators in Optics and Photonics*. CRC Press, 2009.

[3] Dr. Rudiger Paschotta. Finesse. `http://www.rp-photonics.com/finesse.html`, April 2011.

[4] Wikipedia. Whispering gallery. `http://en.wikipedia.org/wiki/Whispering_gallery`, April 2011.